Three-dimensional imaging and numerical reconstruction of graphite/epoxy composite microstructure based on ultra-high resolution X-ray computed tomography

M.W. Czabaj[1*], M.L. Riccio[2], W.W. Whitacre[3]

[1] NASA Langley Research Center, Hampton, VA 23452
[2] Institute of Biotechnology, Cornell University, Ithaca, NY 14853
[3] Draper Laboratory, Cambridge, MA 02139
*Corresponding author (michael.w.czabaj@nasa.gov)

Abstract

A combined experimental and computational study aimed at high-resolution 3D imaging, visualization, and numerical reconstruction of fiber-reinforced polymer microstructures at the fiber length scale is presented. To this end, a sample of graphite/epoxy composite was imaged at sub-micron resolution using a 3D X-ray computed tomography microscope. Next, a novel segmentation algorithm was developed, based on concepts adopted from computer vision and multi-target tracking, to detect and estimate, with high accuracy, the position of individual fibers in a volume of the imaged composite. In the current implementation, the segmentation algorithm was based on Global Nearest Neighbor data-association architecture, a Kalman filter estimator, and several novel algorithms for virtual-fiber stitching, smoothing, and overlap removal. The segmentation algorithm was used on a sub-volume of the imaged composite, detecting 508 individual fibers. The segmentation data were qualitatively compared to the tomographic data, demonstrating high accuracy of the numerical reconstruction. Moreover, the data were used to quantify a) the relative distribution of individual-fiber cross sections within the imaged sub-volume, and b) the local fiber misorientation relative to the global fiber axis. Finally, the segmentation data were converted using commercially available finite element (FE) software to generate a detailed FE mesh of the composite volume. The methodology described herein demonstrates the feasibility of realizing an FE-based, virtual-testing framework for graphite/fiber composites at the constituent level.

INTRODUCTION

Three-dimensional imaging combined with numerical modeling of fiber reinforced polymer (FRP) composites at the constituent (i.e. fiber) length scale holds promise of significantly improving overall understanding of how these complex material systems deform, damage, and ultimately fail. This knowledge can eventually be incorporated into a multiscale "physical and virtual testing" framework [1-7], which will 1) enable discovery of new stochastic- and physics-based damage models, 2) reduce reliance on pure empiricism in design and certification of FRP structures [1,3], 3) enable development of revolutionary structural-life prognosis tools like the Airframe Digital Twin [8], and 4) enable accelerated discovery of new ultra-resilient multifunctional composites.

In the past, 3D imaging and numerical modeling of "non-idealized" FRP microstructures has been restricted by reliance on surface-based imaging techniques (e.g. destructive sectioning coupled with optical and scanning-electron microscopy)

1

and by high computational costs associated with detailed 3D numerical simulations. However, rapid advances in non-destructive 3D micro- and nano-scale X-ray based imaging techniques[1] [9-14] and ongoing improvements in existing supercomputing hardware and numerical algorithms [8,15,16] are beginning to provide a means of overcoming such restrictions.

Recently, a number of notable experimental studies have demonstrated the capability of high-resolution X-ray computed tomography (CT) techniques to visualize microstructure, micro-scale deformation, and damage in various fiber reinforced composites. For example, Latil et al. [17] used synchrotron radiation computed tomography (SRCT) to visualize in-situ 3D deformation of a fluorocarbon fiber bundle (with single fiber dia. of 150 μm) saturated with oil and subjected to transverse compression. In this study, image analysis was used to quantify position, orientation, displacement, and contact of individual fibers within the deforming bundle. In another study, Wright et al. [10] used sub-micron resolution SRCT to visualize post-mortem resin cracking and fiber rupture around a semi-circular notch in an aerospace-grade graphite/epoxy composite tensile coupon. In a later study, Wright et al. [12] utilized the same imaging technique to observe in-situ, micro-scale damage evolution in a double edge notched sample loaded in uniaxial tension. Perhaps the most impressive of these studies is the one conducted by Bale et al. [18], which utilized 1.3 μm resolution SRCT to visualize, in-situ, the sequence of microcracking in SiC-based composites subject to tensile loading at temperatures above 1600 °C.

There are a number of other excellent examples of leveraging 2D and 3D imaging techniques (e.g. from X-ray CT) and numerical simulations across various length scales and material systems. For several examples of such approaches applied to composites, cellular materials, and biomaterials the reader is referred to a review article by Okereke et al. [7]. For recent examples of microstructural imaging of metallic materials using high-energy X-ray diffraction microscopy (HEDM) and supercomputer simulations based on HEDM data, the reader is referred to Refs. [19,20].

To the author's knowledge, converting X-ray CT derived, *constituent-level* FRP data into *high-fidelity*, 3D numerical models has not yet been described in the literature. Until recently, most 2D and 3D microstructural finite element (FE) models have been created based on idealized or statistically-representative fiber arrangements (e.g. [21-30]), or based on 2D scanning-electron or optical microscopy image data (e.g. [25]). In the case of most 3D FE models, a 2D representation of the microstructure is simply extruded along the fiber-length direction to create the third dimension. While these approaches may prove very valuable in some cases (e.g. for modeling deformation and damage of relatively straight, unidirectional composites), they do not reflect the inherent variability in real FRP composites. Inclusion of 3D details, like precise fiber spacing, fiber waviness and misalignment, resin flaws, and foreign debris in numerical models may prove critical in fully realizing a multiscale virtual-testing framework [1].

Despite recent advances in high-resolution X-ray CT imaging techniques, conversion of X-ray CT-derived data into high-quality, realistic, numerical models of actual aerospace-grade FRP composites remains a significant challenge. One reason is that most available methods for converting 3D X-ray CT data (e.g. 3D stack of 2D gray-scale digital images) into numerical models (e.g. using gray-scale

[1] For example, 3D imaging using X-ray computed tomography (CT) is now possible at resolutions as high as ~25-50 nm/voxel)

thresholding) rely on a significant contrast in the attenuation coefficient between individual phases of the imaged material. However, for two-phase material systems like graphite/epoxy composites imaged at ~0.5-1.0 μm resolution[2], the relatively low contrast between fibers and resin, small fiber diameter (~5-7 μm), varying cross-sectional size and shape of individual fibers (e.g. AS4, T300 fibers), and dense packing (fiber volume fraction ~55-67%) render most phase-segmentation-based conversion codes inadequate.

In light of the above, the work described herein and in the companion study [31] demonstrates a combined experimental and computational framework aimed at high-resolution 3D imaging, visualization, and numerical reconstruction of FRP microstructures at the fiber length-scale. To this end, this study adopts concepts from computer vision and multi-target tracking to detect and estimate, with high accuracy, the position of individual fibers in a volume of a graphite/epoxy composite imaged using a 3D X-ray microscope.

In what follows, this manuscript begins with a description of the graphite/epoxy specimen followed by details of the 3D X-ray microscopy imaging. Next, the detection/estimation framework, including the template matching and fiber-tracking/assignment algorithms are presented, followed by a description of FE mesh generation. The manuscript is concluded by presenting results from the reconstruction, statistical quantification of the microstructure, and FE meshing.

MATERIAL SYSTEM AND SPECIMEN PREPARATION

The material system used in this study was a 24 ply, unidirectional, AS4/3501-6 graphite/epoxy composite with a nominal single-ply thickness of 0.132 mm and average fiber diameter of 6.77 ± 0.28 μm. The specimen thickness was chosen to include at least 2-3 plies of the AS4/3501-6 composite while remaining thin enough to maintain quality of the scan and reduce scan time. The resulting "matchstick-type" specimen depicted in Fig.1a had final dimensions of 0.46 mm × 0.33 mm × 20.0 mm in the width (x), thickness (y), and length (z) directions, respectively. The z-direction corresponds to the fiber-length direction. Prior to X-ray CT scanning, the sample was adhered to a small finishing nail and mounted in the X-ray microscope as shown in Fig. 1b.

3D X-RAY MICROSCOPY

The 3D X-ray microscopy was performed using an Xradia 500 Versa[®3] 3D X-ray microscope at the Cornell University Biotechnology Resource Center Imaging Facility. The scan was performed over a 360º rotation using 4000 projections, 60 kV voltage, 5 W power, 14 s exposure time, and 40X objective lens. The resulting voxel size was approximately 460 nm and the total scan time was 16 hours.

Reconstruction of the attenuation data was performed using filtered back-projection, producing a stack of 949 cross-sectional, gray-scale digital images. The resulting cylindrical volume of the composite, depicted in Fig. 2, was 414 μm in diameter and 418 μm in height. For the purpose of subsequent algorithm and code development, a smaller, 169×169×169 μm sub-volume (approximate size of the cross-section shown with red dashed lines in Fig. 2) was extracted and used throughout this work. The sub-volume, the dimensions of which are approximately

3

50 times the average AS4-fiber radius, was chosen to be statistically representative of the bulk composite [23].

THE FIBER SEGMENTATION ALGORITHM

The fiber segmentation algorithm described herein is divided into two steps, both implemented in Matlab$^{®4}$. In the first step, a template-matching (TM) algorithm is used to detect (or "measure") the 2D coordinates of individual-fiber centroids in each cross-sectional image that composes the volume shown in Fig. 2. In the second step, a multi-fiber assignment and tracking algorithm uses the TM detection data to determine 3D coordinates of individual fibers within the imaged volume. A description of each step is presented in the following two sub-sections. For a more detailed discussion of the assignment and tracking algorithm, the reader is referred to a companion study by Whitacre and Czabaj [31].

Template Matching Algorithm

For each 2D cross-sectional image in the 3D stack of tomographic images, the centroid coordinates of individual fibers are detected based on a TM algorithm [32, 33]. This algorithm relies on computation of a normalized cross-correlation (*ncc*) score with the following expression:

$$ncc(x,y) = \frac{\sum_{x,y}[f_I(x,y)-\bar{f}_I][f_T(x,y)-\bar{f}_T]}{\sqrt{\sum_{x,y}[f_I(x,y)-\bar{f}_I]^2 \sum_{x,y}[f_I(x,y)-\bar{f}_T]^2}}, \tag{1}$$

where (x,y) are the pixel coordinates within the cross-sectional image, f_I is the $M{\times}N$ pixel cross-sectional image, f_T is the $m{\times}n$ pixel template, $\bar{f}_I$ is the mean value of the $m{\times}n$ region within f_I centered at (x,y), and $\bar{f}_T$ is the mean value of the $m{\times}n$ template. The summation is performed over the $m{\times}n$ region for both f_I and f_T. Based on Eq. (1), a perfect correlation is obtained when the *ncc* score equals to 1, and perfect anti-correlation is obtained when the *ncc* score equals to -1.

The process of detecting fiber centroids in a 2D cross-sectional image is described sequentially in Fig. 3. For clarity, a small, 70 × 70 µm subset of the entire cross-section (see Fig. 3a) is used in the current discussion. The TM procedure begins with the selection of several templates that are representative of the fiber cross-sections in the entire data set. Selection of individual templates was done by trial-and-error with the aim of maximizing the overall number of true detections, while minimizing the number of false ones. After several iterations, a total of six, 17×17 pixel templates (shown in Fig. 3b), were selected and used throughout this study. Next, the *ncc* score was computed using Eqn. (1) for the entire image seen in Fig. 3a based on template #1. The resulting map of the *ncc* score is shown in Fig. 3c. In this figure, the gray scale corresponds to *ncc* score between -1 (black) and 1 (white). The map of the *ncc* score was then thresholded to values between 0.65-1.0 to remove regions of low correlation. This results in a new image showing local peaks of *ncc* score, as seen in Fig. 3d. Next, a Matlab$^{®}$ function called *imregionalmax* was used to find centers of the local peaks in Fig. 3d. The resulting detections based on template #1 were superimposed onto the original image (Fig.

4

3a) using black crosses, and shown in Fig. 3e. Because a single template typically fails to detect all fiber cross-sections within any given image, the above process was repeated for the remaining five templates. In the final step, detections from all six templates were grouped together using a nearest-neighbor search algorithm with a search radius equal to one-half of the average fiber diameter. The resulting clusters of detections were then averaged, producing a final set of true and spurious detections, as seen in Fig. 3f.

Fiber Assignment and Tracking Algorithm

The TM algorithm generates a set of 2D detections across multiple images that can be used to accurately estimate the number and 3D coordinates of individual fibers throughout the imaged volume. Since the TM algorithm does not always detect all fiber cross-sections within each 2D image composing the 3D volume, and can sometimes generate spurious detections, a robust fiber estimation algorithm is required.

To this end, a multi-fiber tracker based on a Kalman filter [34] is developed. The Kalman filter is a well established approach in target tracking, providing an optimal minimum mean square error estimate when the dynamics and measurements of the tracked object are linear and the errors are Gaussian.

The Kalman filter is divided into predictor and corrector steps. In the prediction step, a fiber cross-section state (e.g. coordinates) in image $k+1$ is estimated based on the state from the previous image, k, using a linear extrapolation model. In the correction step, the new updated state estimate is generated based on an optimal correction using the corresponding TM detection at $k+1$. The assignment between the predicted state estimate and a corresponding TM detection (i.e. from among all possible TM detections at $k+1$) is achieved based on a Global Nearest Neighbor data association scheme [35].

In the current implementation of the fiber assignment and tracking algorithm, it is assumed that for each cross-sectional image the state of each fiber cross-section, x, can be described with a 2D position, $P = [x \; y]$, and velocity, $V = [\dot{x}, \dot{y}]$. Here, V is assumed to be a function of spacing, τ, between two consecutive tomographic images, equal to 460 nm (or 1 pixel). Further, it is assumed that all fibers are continuous and that no two fibers can overlap.

The algorithm begins with the assignment of a unique fiber ID, i, to each detection within the first image, $k = 0$, in the stack. Next, for each detection i in image k, a new state estimate, $\hat{x}_{i,k}$, is initialized:

$$\hat{x}_{i,k} = \begin{bmatrix} x_{i,0} & y_{i,0} & 0 & 0 \end{bmatrix}^T, \tag{2}$$

where $x_{i,0}$ and $y_{i,0}$ are fiber centroid coordinates obtained from the TM algorithm at $k = 0$. In Eqn. (2), it is assumed that each cross-section has zero initial velocity.

After assignment of a unique ID and an initial state to each fiber at k, a new state estimate (or track), $\hat{x}_{i,k+1}$, and covariance matrix, $P_{i,k+1}$, for the next image, $k+1$, are predicted using the standard Kalman filter prediction,

$$\hat{x}_{i,k+1|k} = \Phi\hat{x}_{i,k|k} \tag{3}$$

$$P_{i,k+1|k} = \Phi P_{i,k|k}\Phi^T + Q. \tag{4}$$

5

Note that the notation "$\hat{a}_{c|b}$" represents an estimate of a in image c given observations up to, and including image b. A piecewise constant white acceleration model is used to simulate the change in fiber state between consecutive images [35]. This gives a state transition matrix, $\boldsymbol{\Phi}$, as

$$\boldsymbol{\Phi} = \begin{bmatrix} I_2 & \tau I_2 \\ \boldsymbol{0}_2 & I_2 \end{bmatrix}, \tag{5}$$

and the process noise covariance, $\boldsymbol{Q}$, as

$$\boldsymbol{Q} = \omega \begin{bmatrix} \dfrac{\tau^2}{4} I_2 & \dfrac{\tau^3}{2} I_2 \\ \dfrac{\tau^3}{2} I_2 & \tau^2 I_2 \end{bmatrix}. \tag{6}$$

In Eqns. (5) and (6), I_2 denotes a 2×2 identity matrix, $\boldsymbol{O}_2$ is a 2×2 null matrix, and ω is a process noise scaling factor. In Eqn. (3), the covariance matrix, $\boldsymbol{P}_{i,k+1|k}$, is a measure of the estimated uncertainty of the new predicted state, $\hat{\boldsymbol{x}}_{i,k+1|k}$.

After extrapolation, an assignment step makes the most likely assignment between each of the predicted tracks, $\hat{\boldsymbol{x}}_{i,k+1}$, and the available detections $z_{i,k+1}$ from TM data at $k+1$. In the current implementation, this assignment is based on the Munkres algorithm [36], requiring that it assigns, at most, one detection to a track, and no single detection to more than one track. Additional details of the assignment algorithm are given in [31].

Next, each track that is assigned to a new detection at $k+1$ is corrected with the standard Kalman filter update, given by

$$\boldsymbol{K} = \boldsymbol{P}_{i,k+1|k} \boldsymbol{H}^T \boldsymbol{S}_{i,k+1}^{-1} \tag{7}$$

$$\hat{\boldsymbol{x}}_{i,k+1|k+1} = \hat{\boldsymbol{x}}_{i,k+1|k} + \boldsymbol{K}v \tag{8}$$

$$\boldsymbol{P}_{i,k+1|k+1} = \boldsymbol{P}_{i,k+1|k} - \boldsymbol{K}\boldsymbol{H}\boldsymbol{P}_{i,k+1|k}, \tag{9}$$

where $\boldsymbol{K}$ is the Kalman gain, $\boldsymbol{H}$ is the measurement matrix defined as $\boldsymbol{H} = [I_2\ \boldsymbol{0}_2]$, $\boldsymbol{S}_{i,k+1}$ is the residual covariance defined as $\boldsymbol{S}_{i,k+1} = \boldsymbol{H}\boldsymbol{P}_{i,k+1|k}\boldsymbol{H}^T + \boldsymbol{R}$, $\boldsymbol{R}$ is the measurement error covariance (assumed constant for all measurements), and v is the measurement residual

$$v = \left(\boldsymbol{H}\hat{\boldsymbol{x}}_{i,k+1|k} - \boldsymbol{z}_{i,k+1}\right). \tag{10}$$

The measurement residual measures the discrepancy between the predicted measurement, $\boldsymbol{H}\hat{\boldsymbol{x}}_{i,k+1|k}$ and the assigned measurement $z_{i,k+1}$.

For each track, the process of state prediction and correction described in Eqns. (3)-(10) is repeated over the entire stack of tomographic images. Throughout, any TM detections that did not get assigned to existing tracks are used to initiate new tracks. Additionally, tracks that have missed more than *one* update due to missed detection assignment are removed from further tracking [31]. The resulting set of tracks is next smoothed using a two-pass, forward and backward smoother [37]. Next, all tracks with length less than 169 μm (i.e. ones that do not span the entire volume) are compared to each other to determine which tracks correspond to the same fiber. Tracks that are determined to belong to the same fiber are then stitched together, and once more smoothed. The procedure of smoothing and stitching is repeated several times until there are no remaining fragmented tracks.

In the final step, all fibers are assigned an average fiber diameter of 6.77 μm and the entire data set is examined for possible overlap. In this study, fiber overlap results from errors associated with the TM algorithm, and from inherent variability in diameter of AS4 fibers. Any overlap between pairs of fibers is removed using two additional algorithms. The first algorithm finds fibers with significant overlap (i.e. > 20% of average fiber diameter) and keeps the most likely fibers without overlap. The second algorithm optimally adjusts positions and diameters of all overlapping fibers until all overlap is removed. A detailed description of smoothing, stitching, and overlap removal algorithms is further presented in [31].

FE MESH GENERATION

After fiber segmentation, a multi-step algorithm was used to convert the resulting virtual-fiber data (i.e. coordinates, diameters) into a detailed 3D FE mesh of the composite. First, 3D coordinates of each virtual-fiber were imported into SolidWorks[®5] CAD software and converted into a 3D spline. Next, at the base of each spline, a circle with diameter corresponding to the respective fiber was sketched, and extruded along the spline to create a 3D solid model. The solid model generation was repeated for all segmented fibers using an automated Visual Basic macro routine. The resulting set of individual 3D solid-fibers was converted into a solid model assembly and subsequently imported into Abaqus/CAE[®5] using a binary parasolid file format.

In Abaqus/CAE, a solid bounding box was created around the imported fibers, and a boundary-preserving subtraction/merge routine was used to create a solid region corresponding to the epoxy resin. The subtraction/merge routine enables generation of a coherent mesh between individual fibers and the surrounding resin. The resulting continuous volume, which includes fibers and resin, was seeded and meshed using 3D quadratic tetrahedral (C3D10) elements.

RESULTS AND DISCUSSION

The fiber segmentation algorithm described in the previous section was applied to a 169×169×169 μm sub-volume of the data shown in Fig. 2. The segmented sub-volume was composed from 367 gray-scale images with a z-direction spacing of 460 nm. For this data set, the segmentation algorithm was run on a desktop workstation with a quad-core Intel Core i5-3470, 3.2 GHz CPU with 4 GB of RAM. The computational cost of the entire process including TM, fiber tracking, fiber smoothing, fiber stitching, and overlap removal was approximately 2 hours of wall-clock time. In addition to the automatic segmentation, a graphical-user interface (GUI) algorithm was developed and employed to manually segment 4 undetected fibers, and to remove 3 false tracks.

Within the sub-volume of interest, the fiber segmentation algorithm identified a total of 508 individual fibers. Figure 4 shows a small, 70×70 μm, subset of the segmented volume at different z-coordinates with individual detections (numbered blue circles) overlaid on top of the tomographic data. As seen in Fig. 4, the position of most fiber cross-sections appears to be unchanged with the z-position, indicating good alignment with the z-axis. A few fibers (e.g. 302, 394, 509, 623) appear to be significantly misaligned from the z-axis, as indicated by the rapid change in the x-y

[5] SolidWorks and Abaqus/CAE are registered trademarks of Dassault Systèmes.

coordinates of their respective centroids. Figure 5 shows the entire 169×169×169 µm sub-volume of the imaged composite (Fig. 5a) alongside a solid model rendition of the corresponding fiber segmentation (Fig. 5b). Prior to visualization, the grayscale X-ray CT data in Fig. 5a were thresholded using Avizo$^{®6}$ software to make the regions corresponding to the epoxy resin transparent. The segmented fibers in Fig. 5b were generated, assembled, and visualized in Solidworks$^{®}$ as described in the previous section.

A qualitative (i.e. visual) examination of the data in Figs. 4 and 5 confirms that, within the resolution of the tomographic images, the fiber segmentation algorithm does a very good job of estimating shape and locations of individual fibers within the imaged volume. Additionally, the algorithm appears to accurately capture the size, shape, and distribution of the various resin rich regions. Currently, a more quantitative evaluation of the segmentation algorithm cannot be performed without higher resolution 3D data (e.g. from serial sectioning and optical imaging), which is currently a subject of ongoing research.

After qualitative assessment of the segmentation algorithm, the 3D coordinates of the segmented fibers were used to quantify the relative distribution of individual fiber cross-sections within the imaged sub-volume. To this end, four x-y planes located at $z = 0$, 56, 113, and 169 µm were examined. The first measure of fiber distribution was based on computing the probability distribution function (PDF) of the nearest neighbor distance (NND). The NND is plotted in Fig. 6a as a function of spacing, h, between any two fibers, normalized by the average AS4 fiber diameter, d_{ave}. The second measure was based on computing a radial distribution function, $g(h)$, which is related to the probability of finding a fiber cross-section within a circular annulus with internal radius, h, and thickness, Δh, centered around a reference fiber (shown in Fig. 6b). Several example applications of these two descriptors applied to 2D microstructural data of FRPs are presented in Refs. [26,28,38,39].

Examining both plots in Fig. 6, it is evident that most fibers within the imaged sub-volume are densely packed, with a majority of the fibers clustered within one average fiber-diameter of each other. Examining Fig. 6a, it appears that the probability of finding a nearest-neighbor fiber at $h/d_{ave} < 1$ increases slightly with z, indicating greater fiber compaction at larger z. Qualitatively, this is consistent with the 3D data in Fig. 5, which shows a single diagonal fiber (#623) spanning the volume between $z = 0$ to 103 µm. In this region, the diagonal fiber effectively separates the volume into two distinct regions, decreasing the probability of NND for small z. Examining Fig. 6b, it appears that regardless of z, all fibers tend to cluster at $h/d_{ave} \cong 1$, 2, 3, and 4. For $h/d_{ave} \geq 5$, finding any two fibers away from the reference fiber is equally probable (i.e. $g(h) \rightarrow 1$).

The final quantitative examination of the microstructure was performed by computing an angle, α, which measures misorientation of any given fiber relative to the global z-axis. To simplify this calculation, each fiber was approximated as a straight line that intersects the fiber endpoints, and which is projected onto the x-z plane. The PDF of misorientation relative to the z-axis is presented in Fig. 7a as a function of α. For clarity, the α-axis in Fig. 7a was restricted to angles between ± 5°. To help visualize the fiber z-axis misorientation, the same data were superimposed onto the 3D solid model of the segmented fibers using a color

8

---

scheme as seen in Fig. 7b. In this figure, all fibers with α exceeding $+5^\circ$ were rendered with red color, while fibers with α exceeding -5° were rendered with dark blue color. As evident from Fig. 7, most of the fibers in the upper portion of the volume (i.e. above the red horizontal fiber #623) have slight negative misalignment, while most fibers in the lower portion have a slight positive misalignment. This difference in α between the two regions, along with the presence of a few significantly misaligned fibers in between, suggests that each sub-region corresponds to a distinct ply of the AS4/3501-6 laminate.

In the final step, the segmented fibers depicted in Fig. 5b were imported into Abaqus/CAE® and used to create an FE mesh of the entire composite using the procedure outlined in the previous section. To generate a well-structured, high-quality mesh, a seed density of about 12 elements per fiber perimeter was used throughout. When necessary, Abaqus/CAE® was allowed to adaptively relax the specified element size constraint to account for complex geometrical features (e.g. close spacing and contact between individual fibers). Meshing was performed on a desktop workstation with a quad-core Intel Core i7-3720QM, 3.6 GHz CPU with 32 GB of RAM, with a computation cost of approximately 1 wall-clock hour. The final FE mesh shown in Fig. 8, contained ~6.7 million quadratic, tetrahedral C3D10 elements and ~27 million degrees of freedom (DOF). Considering the scope of this study, no attempts were made to perform a detailed mesh convergence study. However, to explore tractability of the current model, a static, linear-elastic simulation of uniaxial tension (along *y*-axis) was performed with FEAWD[7] parallel FE solver using 1000 Intel Ivy Bridge cores of NASA's Pleiades supercomputer (total 184,800 cores available). The pre- and post-processing of the FE model and the results took several hours; however, the actual static simulation was completed in approximately 140 wall-clock seconds. The same simulation was completed in 55 seconds using 5000 cores.

The combined imaging, segmentation, and meshing procedure described herein provides a significant step towards realizing the idea of virtual testing of FRPs at the constituent scale. However, despite the very promising results shown herein, a number of important technical challenges remain. For instance, in the present study a relatively small, unidirectional matchstick specimen was used to obtain high quality X-ray CT data. For practical applications it may be necessary to acquire such data from larger, macro-scale components with off-axis fiber stacking sequences, over limited scan angles (i.e. $<180^\circ$). As a result, the present segmentation algorithm must be extended to enable processing larger volumes of noisier and perhaps incomplete data. Finally, despite the relatively low computation cost (for a Pleiades-type supercomputer) of performing static, linear-elastic simulations, future inclusion of non-linear effects and damage (e.g. plasticity, fracture) into these models may increase the computational cost dramatically. With this in mind, new, adaptive-meshing algorithms that generate efficient meshes will have to be developed.

CONCLUSION

This manuscript describes a combined experimental and computational study aimed at high-resolution 3D imaging, visualization, and numerical reconstruction of fiber reinforced polymer microstructures at the fiber length-scale. To this end, a

[7] FEAWD was developed at the Cornell University Fracture Group (www.cfg.cornell.edu).

small sample of graphite/epoxy composite was imaged at sub-micron resolution using a 3D X-ray computed tomography microscope. Next, a novel segmentation algorithm was developed based on concepts adopted from computer vision and multi-target tracking to detect and estimate, with high accuracy, the position of individual fibers in a volume of the imaged composite. In the current implementation, the segmentation algorithm was based on a Global Nearest Neighbor data-association architecture, a Kalman filter estimator, and several novel algorithms for fiber stitching, smoothing, and overlap removal. The segmentation algorithm was demonstrated on a 169×169×169 μm sub-volume of the imaged composite, detecting 508 individual fibers. The segmentation data were qualitatively compared to the tomographic data, demonstrating high accuracy of the numerical reconstruction. Moreover, the data were used to quantify a) the relative distribution of individual fibers cross-sections within the imaged sub-volume, and b) the local fiber misorientation relative to the global fiber axis. Finally, the segmentation data were converted using commercially available finite element (FE) software to generate a detailed finite element mesh of the composite volume. The methodology described herein demonstrates the feasibility of realizing an FE-based virtual-testing framework for graphite/fiber composites at the constituent level.

ACKNOWELDGEMTS

REFERENCES

[1] Cox B, Yang, QD. In Quest of Virtual Tests for Structural Composites. *Science* 2006; 314:1102-1107.

[2] Cox B, Spearing SM, Mumm DR. Practical Challenges in Formulating Virtual Tests for Structural Composites. In: Camanho PP, Davila CG, Pinho ST, editors. Dordrecht: Springer Science and Business Media; *Mechanical Response of Composites* 2008; 10:57-75.

[3] Hallet SR, et al. The Open Hole Tensile Test: a Challenge for Virtual Testing of Composites. *International Journal of Fracture* 2009: 158(2):169-181.

[4] Yang QD, Cox BN, Fang XJ, Zhou ZQ. Virtual Testing for Advanced Aerospace Composites: Advances and Future Needs. *J Eng Mater Technol* 2010; 133(1):1-6.

[5] LLorca J, González C, Molina-Aldareguía JM, Lópes CS. Multiscale Modeling of Composites: Toward Virtual Testing… and Beyond. *JOM* 2013; *65*(2):215-225.

[6] Cox B, Bale H, Blacklock M. A Pipeline Approach to Developing Virtual Tests for Composite Materials. *13th International Conference on Fracture*, Beijing, China. June 16-21, 2013.

[7] Okereke MI, Akpoyomare AI, Bingley MS. Virtual Testing of Advanced Composites, Cellular Materials and Biomaterials: a Review. *Composites Part B: Engineering* 2014; 60:637-662.

[8] Tuegel E, Ingraffea A, Eason Y, Spottawood S. Reengineering Aircraft Structural Life Prediction Using a Digital Twin. *Int J Aeros Eng* 2011; 2011:1-14.

[9] Feser M, Gelb J, Chang H, Cui H, Duewer F, Lau SH, Yun W. Sub-micron Resolution CT for Failure Analysis and Process Development. *Measurement science and technology* 2008; 19(9):1-8.

[10] Wright P, Fu X, Sinclair I, Spearing SM. Ultra High Resolution Computed Tomography of Damage in Notched Carbon Fiber-Epoxy Composites. *Journal of composite materials* 2008; 42(19):1993-2002.

[11] Kirz J, Jacobsen C. The History and Future of X-ray Microscopy. *In J Phys Conf Ser* September 2009; 186(012001):1-11.

[12] Wright P, Moffat A, Sinclair I, Spearing SM. High Resolution Tomographic Imaging and Modelling of Notch Tip Damage in a Laminated Composite. *Composites Science and Technology* 2010; 70(10):1444-1452.

[13] Merkle A, Gelb J. Recent Advancements in Laboratory X-ray Microscopes enabling 3D and 4D Science. *Microscopy and Microanalysis* 2013; 19(S2):1314-1315.

[14] Merkle AP, Gelb J. The Ascent of 3D X-ray Microscopy in the Laboratory. *Microscopy Today* 2013; *21*(02):10-15.

[15] Simon H, Zacharia T, Stevens R. Modeling and Simulation at the Exascale for Energy and the Environment, *Office of Science, U.S. Department of Energy Technical Report* 2007.

[16] Post D. Computational Science and Engineering Software Development Challenges and Solutions. *Department of Defense High Performance Computing Modernization Program HEC-IWG*, 18 Aug 2011, Arlington, VA.

[17] Latil P, Orgéas L, Geindreau C, Dumont PJ J, Rolland du Roscoat S. Towards the 3D *in situ* Characterisation of Deformation Micro-mechanisms within a Compressed Bundle of Fibres." *Composites Science and Technology* 2011; 71(4):480-488.

[18] Bale HA, Haboub A, MacDowell AA, Nasiatka JR, Parkinson DY, Cox BN, Ritchie RO. Real-time Quantitative Imaging of Failure Events in Materials under Load at Temperatures above 1,600° C. *Nature materials* 2013; *12*(1):40-46.

[19] Herbig M, King A, Reischig P, Proudhon H, Lauridsen EM, Marrow J, Ludwig W. 3-D Growth of a Short Fatigue Crack within a Polycrystalline Microstructure Studied using Combined Diffraction and Phase-contrast X-ray Tomography. *Acta Materialia* 2011; 59(2):590-601.

[20] Spear A. Numerical and Experimental Studies of Three-dimensional Crack Evolution in Aluminum Alloys: Macroscale to Microscale" Ph.D. thesis, Cornell University, 2014.

[21] González C, LLorca J. Multiscale Modeling of Fracture in Fiber-reinforced Composites. *Acta Materialia* 2006; *54*(16):4171-4181.

[22] Rosso P, Váradi K. FE Macro/micro Analysis of Thermal Residual Stresses and Failure Behaviour under Transverse Tensile Load of VE/CF-fibre Bundle Composites. *Composites science and technology* 2006; *66*(16):3241-3253.

[23] Trias D, Costa J, Turon A, Hurtado JE. Determination of the Critical Size of a Statistical Representative Volume Element (SRVE) for Carbon Reinforced Polymers. *Acta Materialia* 2006; *54*(13):3471-3484.

[24] Wongsto A, Li S. Micromechanical FE analysis of UD fibre-reinforced composites with fibres distributed at random over the transverse cross-section. *Composites Part A: Applied Science and Manufacturing* 2005; 36(9): 1246-1266.

[25] Huang Y, Jin KK, Ha SK. Effects of Fiber Arrangement on Mechanical Behavior of Unidirectional Composites. *Journal of composite materials* 2008; *42*(18):1851-1871.

[26] Melro AR, Camanho PP, Pinho ST. Generation of Random Distribution of Fibres in Long-Fibre Reinforced Composites. *Composites Science and Technology* 2008; *68*(9):2092-2102.

[27] Mishnaevsky Jr L, Brøndsted P. Micromechanisms of Damage in Unidirectional Fiber Reinforced Composites: 3D computational analysis. *Composites Science and Technology* 2009; *69*(7):1036-1044.

[28] Vaughan TJ, McCarthy CT. A Combined Experimental–Numerical Approach for Generating Statistically Equivalent Fibre Distributions for High Strength Laminated Composite Materials. *Composites Science and Technology* 2010; *70*(2):291-297.

[29] Canal LP, González C, Segurado J, LLorca J. Intraply Fracture of Fiber-Reinforced Composites: Microscopic Mechanisms and Modeling. *Composites Science and Technology* 2012; *72*(11):1223-1232.

[30] Okereke MI, Akpoyomare AI. A Virtual Framework for Prediction of Full-Field Elastic Response of Unidirectional Composites. *Computational Materials Science* 2013; *70*:82-99.

[31] Whitacre WW, Czabaj MW. Automated 3D Digital Reconstruction of Fiber Reinforced Polymer Composites. *AIAA Guidence, Navigation, and Control Conference*, Kissimmee, Florida 2015.

[32] Nicholson WV, Glaeser RM. Review: Automatic Particle Detection in Electron Microscopy. *Journal of structural biology* 2001; 133(2):90-101.

[33] Zabulis X, Papara M, Chatziargyriou A, Karapantsios TD. Detection of Densely Dispersed Spherical Bubbles in Digital Images Based on a Template Matching Technique: Application to Wet Foams. *Colloids and Surfaces A: Physicochemical and Engineering Aspects* 2007; 309(1):96-106.

[34] Kalman, RE. A New Approach to Linear Filtering and Prediction Problems. *Transactions of the ASME – Journal of Basic Engineering* 1960; pp. 35-45.

[35] Blackman, SS, Popoli, R. Design and Analysis of Modern Tracking Systems, Artech House; Boston MA, 1999.

[36] Munkres J. Algorithm for the Assignment and Transportation Problems. *Journal of the Society for Industrial & Applied Mathematics* 1957; 5(1): 32–38.

[37] Bar-Shalom Y, Li XR, Kirubarajan T. Estimation with Application to Tracking and Navigation, John Wiley and Sons, 2001.

[38] Buryachenko VA, Pagano NJ, Kim RY, Spowart JE. Quantitative Description and Numerical Simulation of Random Microstructures of Composites and Their Effective Elastic Moduli. *International Journal of Solids and Structures* 2003; 40(1):47-72.

[39] Romanov V, Lomov SV, Swolfs Y, Orlova S, Gorbatikh L, Verpoest I. Statistical Analysis of Real and Simulated Fibre Arrangements in Unidirectional Composites. *Composites Science and Technology* 2013; (87):126-134.

FIGURES

(a) (b)
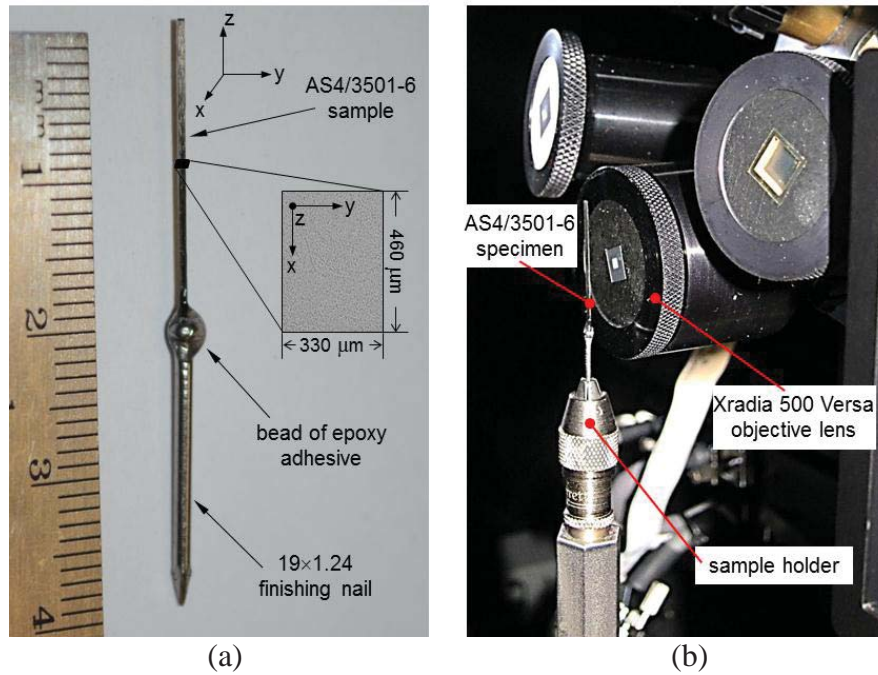
Fig. 1 The AS4/3501-6 specimen a) prior to scanning and b) mounted inside Xradia 500 Versa[®] microscope.
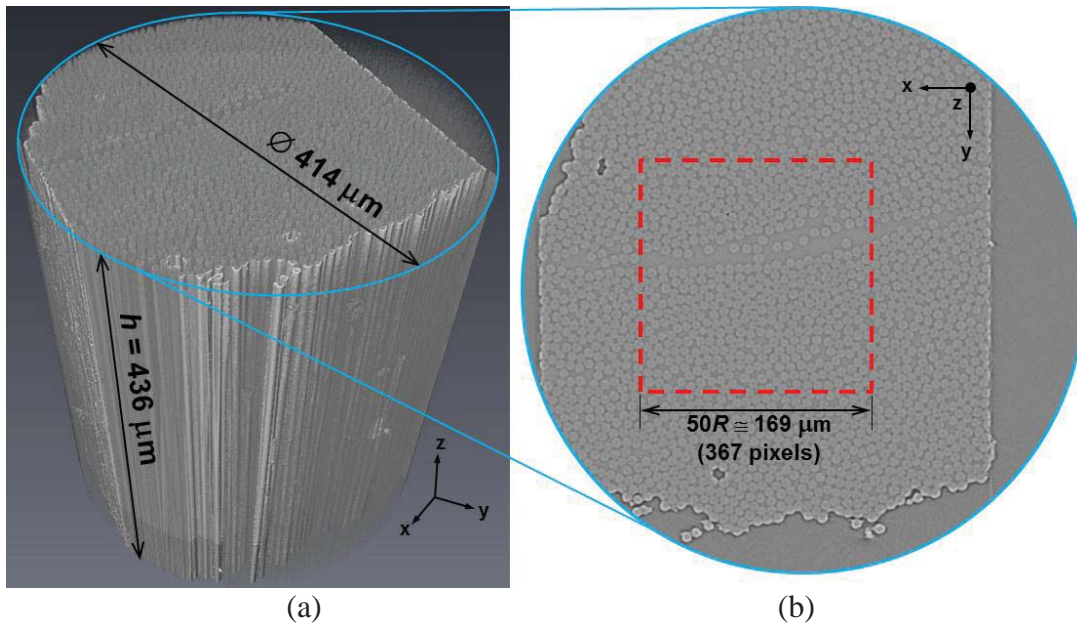
Fig. 2 AS4/3501-6 graphite/epoxy specimen: a) reconstructed volume and b) cross-sectional image with sub-volume selected for numerical reconstruction outlined in red dashed box.
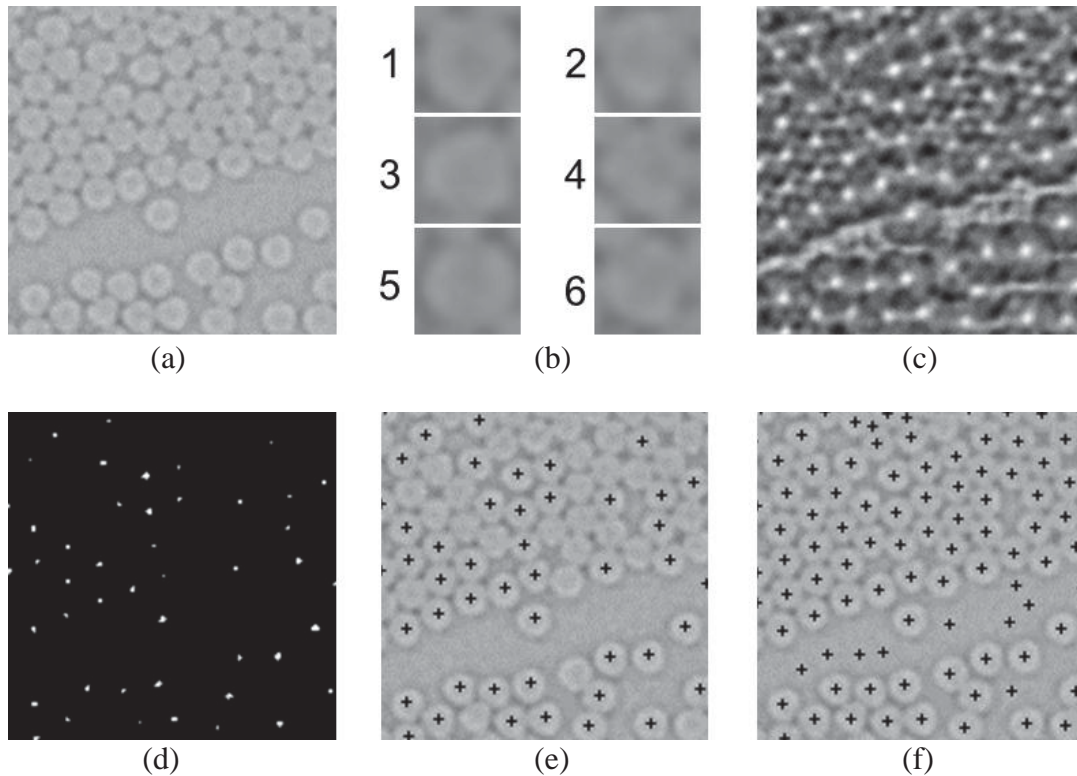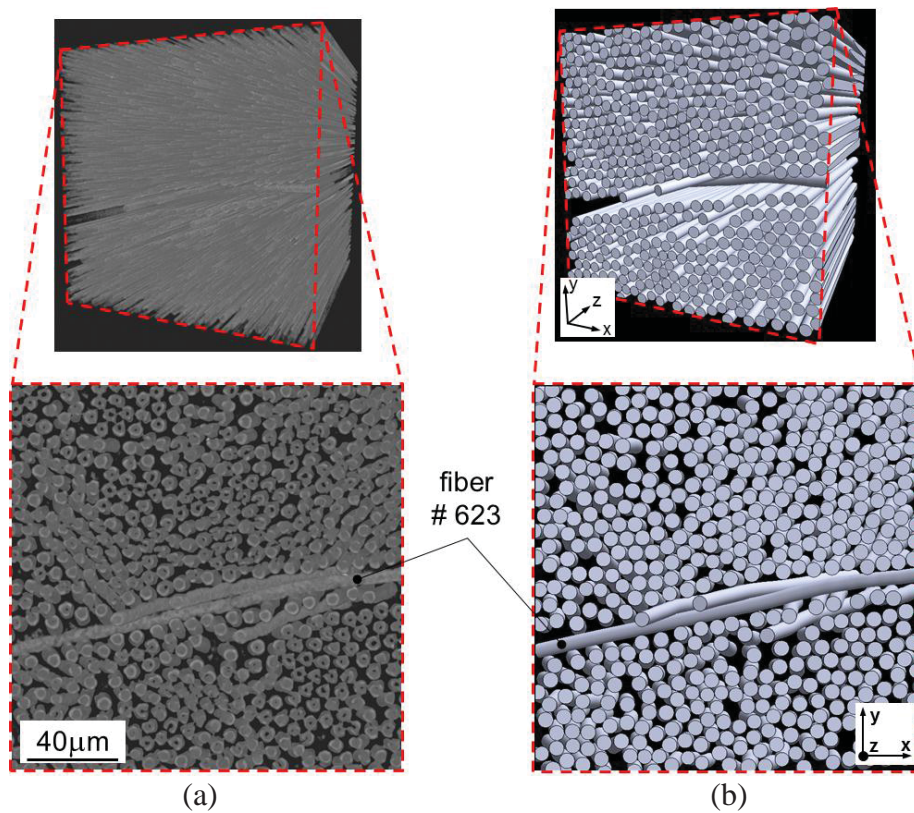

Fig. 3 Sequence of images describing the TM algorithm: a) 2D X-ray CT image, b) six fiber templates, c) map of *ncc* score from template #1, d) map of *ncc* score after thresholding, e) detections from template #1, f) detections from templates # 1-6.
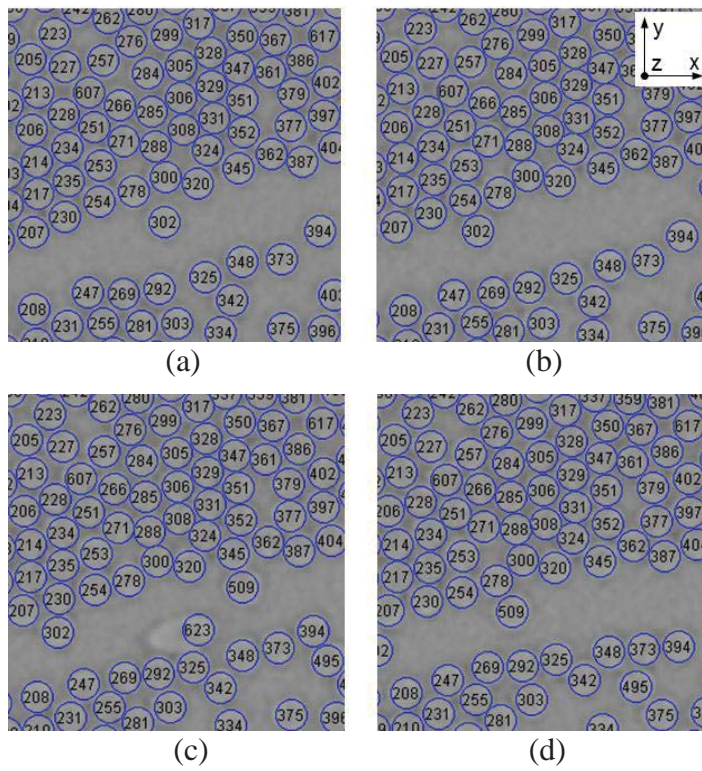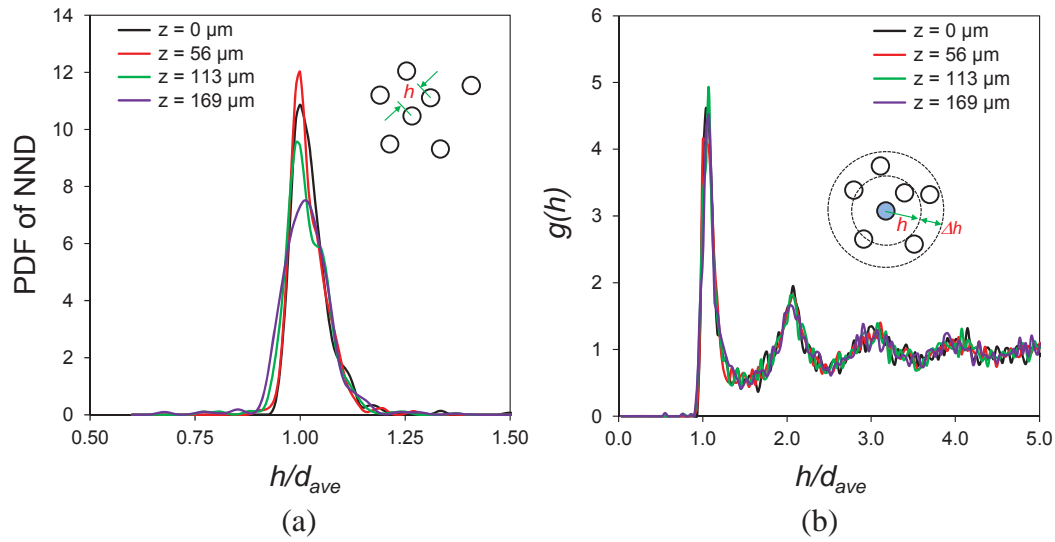
Fig. 4 Example of tracked fibers (blue circles) overlaid on top of the X-ray CT data at a) $z = 0$ µm, *b*) z = 56 µm, *c*) z =113 µm, and *d*) z = 169 µm.


Fig. 5 3D rendition of (a) the X-ray CT data, and (b) solid model representation of the segmented fibers.

Fig. 6 Statistical description of fiber arrangement at different *z*-coordinates based on a) the nearest neighbor distance and b) radial distribution function.
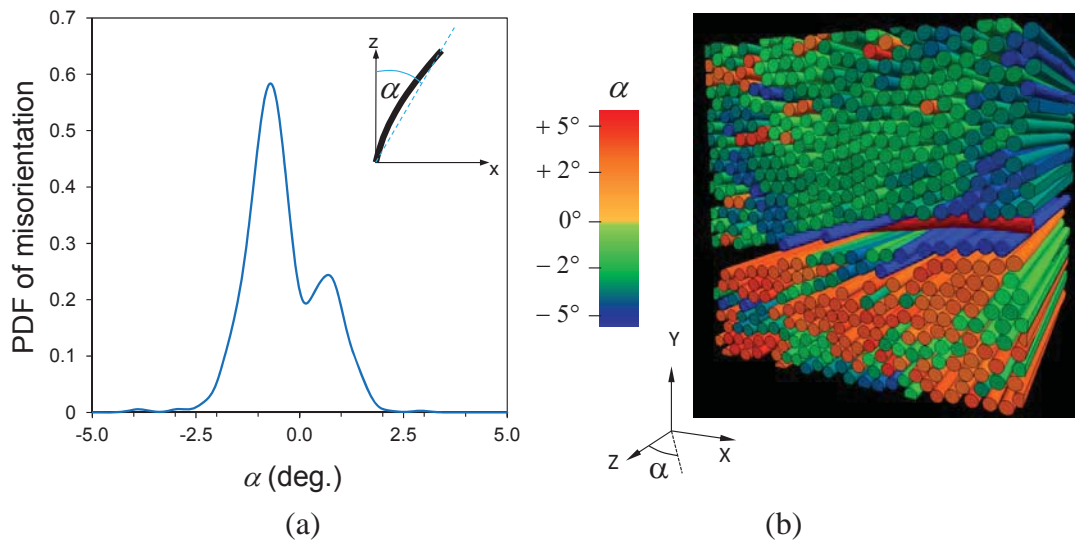
Fig. 7 (a) PDF of fiber misalignment relative to the *z*-axis, and (b) 3D CAD rendition of the segmented fibers with color scheme representing the misalignment angle, α.
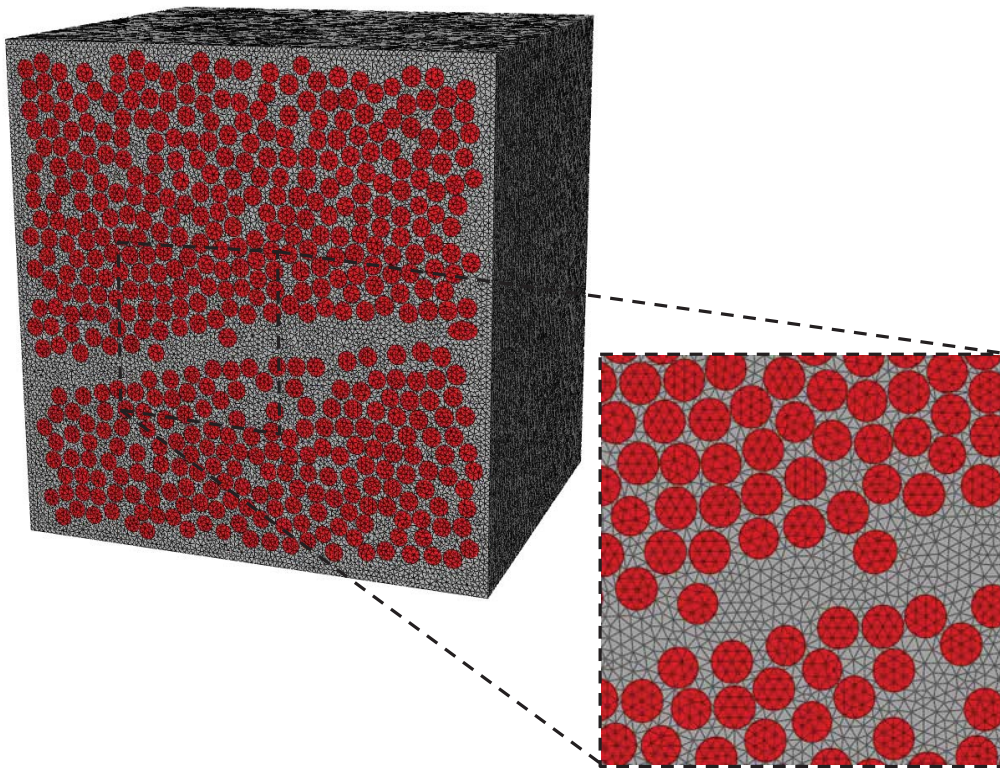
Fig. 8 Finite element mesh created using Abaqus/CAE® (~6.7M tetrahedral elements, ~27M DOF).